Nanoporous Microtubes obtained from a Cu-Ni Metallic Wire

Nanoporous Microtubes obtained from a Cu-Ni Metallic Wire

Emanuele Francesco Marano, Danilo Lussana[#] Alberto Castellero*, Marcello Baricco

Department of Chemistry and NIS, University of Turin, Turin, Italy

[#] Current address: Cogne Acciai Speciali Spa, Aosta, Italy

* Corresponding author. Tel.: +39 0116707097; fax: +39 0116707855; e-mail: alberto.castellero@unito.it

Abstract

Nanoporous microtubes of a nickel-copper alloy were obtained from a Cu-44Ni-1Mn (wt.%) wire (200 μm diameter). A new synthesis method was established through three steps: 1) partial oxidation of the wire at 1173 K in air, 2) removal of the inner unoxidized core by chemical etching, 3) reduction in 10 bar hydrogen atmosphere.

During oxidation, the segregation of Cu and Ni occured because of their different diffusion coefficients in the corresponding oxides. As a consequence, pores were formed by Kirkendall effect and due to selective chemical etching of the different oxides. Additional porosity formed because of volume contraction during reduction with hydrogen.

The process allowed to obtain microtubes with tuneable wall thickness and inner pores around 180 ± 80 nm. The morphological features developed suggest improved capillarity properties for applications in MEMS.

Keywords: alloys; porous materials; oxidation; diffusion; segregation; X-ray diffraction

1. Introduction

Microtubes with fine tuneable thickness are typically synthesized by electroforming or sputtering, using a sacrificial support [1-3]. They are used as microneedles [4] and for applications in Micro Electro Mechanical Systems (MEMS) [5], gas sensing [6], lasers, optical, semiconductor and biomedical devices [2,5]. Microtubes obtained by electroforming are compact and have smooth surfaces. Conversely, microtubes with nanoporous walls show enhanced capillarity properties and specific surface properties, leading to potential applications in MEMS for fluid transport or sensing [7,8,9].

Nanoporous materials can be obtained by several routes such as selective dissolution, dealloying, reduction of metal oxides and Kirkendall effect [10,11,12]. Methods based on selective dissolution and dealloying require that the reduction potentials of the components are well separated, so that the less noble components are soluble in the oxidized state while the most noble component remains in the metallic state. An example of porous material obtained by selective dissolution is Raney catalyst where, under highly basic conditions, Al is chemically dissolved from AlNi alloy and Ni is oxidized on the surface. As a consequence, Ni is not surface mobile, limiting Raney catalyst to the powder form [13].

In the case of dealloying, the more noble non oxidized element is free to diffuse at the alloy/electrolyte interface, allowing the formation of a continuous porous material [10]. For instance, porous Au, Pd and Cu were obtained by dealloying of Ag-Au, Ag-Pd and Cu-Mn, respectively [14-16]. More recently, dealloying of Au-based amorphous alloys allowed to obtained nanoporous gold which can be used as substrate for surface-enhanced Raman scattering **[17].**

In the case of oxides, mesoporous MnO can be obtained by a template free route starting from $ZnMn_2O_4$, where Zn is selectively reduced and subsequently expelled in vapour phase [11].

Up to date, processing of nanoporous materials is widely studied and models for pore formation have been proposed [10-18]. Conversely, few works can be found on the preparation of porous metallic microtubes (see for example Ref. [19]).

In this work, different methods, that are typically used for processing nanoporous materials, are combined in order to obtain a nanoporous metallic microtube starting from a commercial constantan (i.e. Cu-Ni alloy) wire. At first, the metallic wire is partially oxidized, then it is chemically etched for the removal of the un-oxidized inner core, and, finally, the oxide microtube is reduced in hydrogen atmosphere. Final microtubes (about 230 μm in outer diameter) show tuneable wall thickness, depending on the oxidation time, and inner pores around 180 ± 80 nm.

Pores formation is explained by segregation of ions with different mobility during oxidation of the bimetallic alloy (i.e. Kirkendall effect), selective removal of the different oxides during chemical etching and volume contraction during reduction with hydrogen.

2. Experimental procedures

A polyurethane-enamelled 200 μm diameter constantan wire from Gebaur&Griller with nominal composition Cu-44Ni-1Mn (wt.%), corresponding to $Cu_{53}Ni_{46}Mn_1$ (at.%), was used as starting material. In the first step, the material was cut in 3-5 cm long pieces and placed in air in a pre-heated muffle oven at 1173 K inside alumina crucibles. The wires were exposed to the oxidation atmosphere for the following times: 5, 10, 20, 40, 80, 160 and 1440 minutes.

In the second step, chemical etching with 65% nitric acid at room temperature allowed to remove the inner metallic core leaving intact the external oxide layer with formation of a microtube.

Finally, reduction of the microtubes was performed by heating the samples from room temperature to 723 K at 10 K/min under 10 bar of hydrogen inside a Differential Scanning Calorimeter (DSC) Netzsch DSC HP-204, using aluminium pans as sample holders.

Thermodynamic properties of the reactions involved were calculated using the Thermocalc software and the database “Substance” [20].

The thickness of the oxide layer after oxidation for different times was measured by optical microscopy observations (Leica DMLM) across the transversal section of the samples. Scanning Electron Microscopy (SEM) observations were performed using a Leica Steroscan 410 equipped

with an Oxford Instruments INCAx-sight probe for Energy Dispersive X-ray analysis (EDX). X-ray diffraction (XRD) measurements were performed with a Philips X'Pert Pro (Cu Kα) equipped with a X'Celerator detector. The XRD patterns were collected using a step size of 0.0167° and a capillary spinner setup with a 0.3 mm diameter glass capillary. The capillary containing the sample was aligned with the help of a microscope with a graduated scale in order to minimize the displacement of the sample from the focus plane. Rietveld refinement was performed in order to determine the lattice parameters of the crystal phases using the software MAUD [21]; because of the capillary and sample geometries, it was not possible to evaluate the relative quantity of the observed phases.

3. Results and discussion

On the basis of the thermodynamic analysis, it turns out that oxidation in air of Cu-Ni alloys and subsequent reduction in H_2 atmosphere are spontaneous reactions, indicating that constantan is a suitable material for the aim of this work.

Fig. 1(a) shows the optical micrograph of the transversal cross sections of the wires oxidized at 1173 K for different times. Samples oxidized for short times (5 min and 10 min) show a thin and easily separable layer of oxide. The sample oxidized for 1440 minutes (24 hours) was fully oxidized. Fig. 1(b) reports the mean values of the square oxide thickness as a function of the oxidation time. Data points are calculated by averaging thickness measurements of the oxide in different positions in the same cross section and in different cross sections of the same sample. The error bars are the standard deviation of the averages. The kinetic of oxidation can be described by a parabolic law ($x^2 = K_p t$, where x, K_p and t are oxide thickness, parabolic rate constant and oxidation time, respectively) for the early stage of the process, as shown by the continuous line in Fig. 1(b) obtained by fitting the experimental data from 0 min to 80 min. The estimated value of K_p for the early stage of oxidation is $8.7\ 10^{-8}\ g^2\ cm^{-4}\ s^{-1}$. Such a value is comparable with those reported in the literature for alloys with similar composition (e.g. for $Cu_{50}Ni_{50}$ $K_p = 0.2\ 10^{-8}\ g^2\ cm^{-4}\ s^{-1}$ at 1073 K [2] and $K_p = 5.0\ 10^{-8}\ g^2\ cm^{-4}\ s^{-1}$ at 1098 K [23]). For longer oxidation time (i.e. 160 min) the

oxidation rate becomes faster (i.e. increase of K_p) with respect to the earlier stage, represented by the dotted line. According to the literature, such an increase of the oxidation rate has been related to a complex oxidation mechanism that involves the formation of multi-layered oxide scales [23-25]. Samples oxidized for 20, 40, 80 and 160 minutes show an external porous layer with uniform thickness. For the sample oxidized at 1173 K for 160 minutes, the oxide layer is thick enough to obtain, after chemical etching, a mechanically self-standing microtube that can be easily handled for the subsequent steps. Therefore, only the results obtained for this sample will be presented in this work.

In Fig. 1(c), the backscattered electrons SEM image of the cross section of the sample oxidized for 160 min shows a darker porous external layer and a brighter compact inner core, corresponding to the oxidized and the un-oxidized alloy, respectively. The EDX compositional map in Fig. 1(d) reveals the elemental distribution of Cu (red), Ni (green) and Mn (blue) in the same area shown in Fig. 1(c). A clear segregation of copper oxide in the external part of the wire is visible, while the layer underneath is richer in nickel (as an oxide) with respect to the original alloy composition. Furthermore, at the interface between the alloy and the oxidized Ni-rich layer, a red metallic copper layer can be observed. The thickness of this layer increases with the oxidation time, as shown in Fig. 1(a).

As discussed in ref. [22], Cu and Ni are segregated during oxidation of Cu-Ni alloys because of the much larger lattice diffusion coefficient of Cu in Cu_2O with respect to that of Ni in NiO (at 1173 K, ~10^{-9} cm^2s^{-1} [26] and ~10^{-13} cm^2s^{-1} [27], respectively). The different mobility of the metallic ions in the corresponding oxides generates an excess of vacancies that tend to coalesce, leading to the formation of pores according to the Kirkendall effect, as often observed in the oxidation process of bimetallic alloys, such as alpha brass [28].

Fig. 2(a) shows the XRD pattern at each synthesis step, together with the corresponding Rietveld refined pattern. The master alloy shows the typical face-centered cubic (f.c.c.) structure of the metallic solid solution of nickel and copper, as expected from the Cu-Ni phase diagram [29], with a

lattice parameter a = 3.573 Å. On the basis of the Vegard law [30] applied to the Cu-Ni system and excluding the presence of Mn, a composition of $Cu_{54}Ni_{46}$ (at.%) was estimated for the solid solution, in agreement with the nominal composition of the wire. Texture effects, due to the cold drawing process employed in the wire manufacturing process, are clearly observed.

In the oxidized sample, Fig. 2(a), NiO, CuO and Cu_2O were found to be the constituents of the oxide layer, while only the most intense peaks of the f.c.c. solid solution are still observable (at 2θ around 44° and 51°). The relative intensities of the residual metallic solid solution do not match those of the master alloy because textures present in the original wire are removed during the thermal treatment performed during oxidation. From the value of the lattice parameter of NiO (a = 4.200 Å), a Cu content in the oxide of about 25 % at. was estimated [31], in agreement with the solubility range of Cu in NiO [32].

According to XPS spectra [33], FTIR and SIMS analysis [34], NiO and Cu_2O form simultaneously on the surface. Subsequently, on the external surface, Cu(I) oxidizes to Cu(II) because of thermodynamic reasons, and segregates because of kinetic reasons. Conversely, at the metal/oxide interface, Cu_2O oxidizes Ni in the metallic solid solution [24, 25, 33, 34], forming the observed metallic copper layer, according to the reaction

$$Cu_2O + Ni \rightarrow 2Cu + NiO \quad (1)$$

that is spontaneous at 1173 K (ΔG = -51.3 kJ/mol).

According to this mechanism and on the basis of SEM and XRD analysis (Fig. 1(c-d) and Fig. 2(a), respectively), it can be inferred that the external layer, marked in red in Fig. 1(d), is prevalently constituted by CuO and that the inner oxidized layer is mainly a mixture of NiO (with dissolved Cu) and Cu_2O.

The XRD pattern of the partially oxidized sample after HNO_3 etching, Fig. 2(a), shows only peaks of the oxide phases and the disappearance of the weak crystallographic reflections related to the master alloy because of the removal of the metallic inner core. After etching, the relative intensity of the Cu_2O peaks decreases significantly, suggesting a partial removal of this phase. This step

contributes to the development of porosity, because of the selective removal of the metallic copper at the metal-oxide interface and Cu_2O in the mixed NiO phase.

As an example, the DSC trace for the sample oxidized at 1173 K for 160 minutes is reported in Fig. 3. During reduction under 10 bar of H_2, DSC traces show two overlapped exothermic peaks with the onset temperatures falling at about 470 K and 550 K for all samples. On the basis of the XRD analysis (not shown here) performed on samples annealed just after the first exothermic peak and to the end of the whole DSC scan, it was possible to assign the first signal to the reduction of CuO and the second signal to the reduction of NiO.

SEM images of the reduced sample, Fig. 4(a-c), show a rather uniform thickness of the microtube wall (63 - 68 μm) and a concentric multilayered morphology. The detachment of the inner layer can be explained by the shrinkage of the material during the reduction in hydrogen atmosphere, due to the different densities between metals and oxides (8.9 g/cm^3 and about 6.5 g/cm^3, respectively). Pores, intended as voids between particles, are spread across the whole section of the microtube wall. The dimensions of particles between voids vary from 180 ± 80 nm for the inner layer, Fig. 4(c), to about 1.50 μm and more for the external layers. Fig. 4(d) shows the EDX composition profile as a function of the distance from the inner side of the microtube. Mn concentration is uniform along the whole cross section, showing that segregation does not occur for this element. The composition varies continuously and almost linearly from 98 at.% Ni to about 70 at.% Ni in the first 50 μm of the wall. Afterwards, a sharp compositional boundary marks the transition to the external Cu-rich region (about 10 μm thick) containing up to 97 at.% Cu. In correspondence of the observed compositional boundary a morphological counterpart is not observed, as shown by the SEM images, Fig. 4(a-b). The EDX composition profile, Fig. 4(d), suggests the presence of a solid solution which continuously changes its composition.

The XRD pattern after reduction, Fig. 2(a), confirms the disappearance of the oxide phases and the appearance of two f.c.c. metallic phases, named f.c.c.(1) and f.c.c.(2) respectively. Fig. 2(b) is an enlarged view of the (311) and (222) peaks of f.c.c.(1) and f.c.c.(2) present in the reduced sample,

showing that the peaks around 92.3° and 97.8°, related to f.c.c.(2), are significantly broader than those around 90° and 95.3°, related to f.c.c.(1). In the case of f.c.c.(1), the value of the lattice parameter, *a*, is 3.610 Å, which corresponds to a composition of $Cu_{95}Ni_5$ (at.%). The broadening of the peaks corresponding to f.c.c.(2) can be caused, in principle, by the presence of nanosized scattering domains, mechanical microstrain or chemical strain due to a continuous chemical gradient. Therefore, in Rietveld refinement, the broad peaks related to f.c.c.(2) phase were fitted according to two different approaches. On the one hand, assuming a single f.c.c. phase, the fitted pattern (green line in Fig. 2(b), with lattice parameter a = 3.554 Å, corresponding to the solid solution $Cu_{34}Ni_{66}$, at.%) is significantly shifted to the left with respect to the experimental one. Furthermore, the values of the crystallites domain size (30 nm) and microstrain (0.005) are respectively too small and too large for a sample in the annealed state. Finally, assuming the presence of a single f.c.c.(2) phase (with a unique value of the lattice parameter and, consequently, a constant composition) is in contrast with the composition gradient observed by EDS analysis, Fig. 4(d). On the other hand, the fit is performed arbitrarily assuming the coexistence of several f.c.c. phases with fixed crystallite size (100 nm) and microstrain (0.0006) with the lattice parameter varying from a = 3.524 Å (i.e. pure Ni) to a =3.594 Å, in order to simulate the presence of a continuous composition gradient. In Fig. 2(b), the red line represents the calculated pattern obtained as the sum of the contributions of eight f.c.c. phases with different lattice parameters and it shows a satisfactory accordance with the experimental pattern. The contribution of the f.c.c. phase with lattice parameter of 3.544 Å, containing about 22 at. % of copper, is the most relevant in intensity and is very close to the maximum of the experimental curve.

According to the EDS and XRD analysis, it turns out that, as a consequence of the segregation of Cu and Ni observed during the oxidation of the master alloy, the final reduced sample is formed by a single Cu-rich phase, f.c.c.(1), and a series of f.c.c.(2) phases richer in Ni with respect to f.c.c.(1), with a continuous composition gradient.

4. Conclusions

In this work a porous metallic microtube was obtained with a simple route. The process requires the partial oxidation of a Cu-44Ni-1Mn (wt.%) wire (commercial constantan) followed by nitric acid etching for the removal of the inner metallic core and subsequent reduction in H_2 atmosphere. The thickness of the wall is tuneable by controlling the oxidation time. The reduced microtube shows a composition gradient from the inner wall (almost pure nickel) to the outer wall (almost pure copper). The boundary between the inner and outer layers is well defined because of the abrupt variation in composition, however there is not a corresponding change in morphology. The transversal section of the microtube shows a gradient of porosity. Segregation of Cu and Ni, occurring in the oxidation step as a consequence of their different diffusion coefficients in the corresponding oxides, leads to pores formation by Kirkendall effect and by selective chemical etching of the different oxides. Additional porosity forms because of volume contraction during reduction with hydrogen.

In future perspective, porosity and pores dimensions can be possibly tuned by varying the mutual composition of the elements in the master alloy.

References

[1] W.P. Hoffman and P.G. Waper, Microscopic tube devices and method of manufacture, patent US6113722A (2000).

[2] G. Chatzipirpiridis, O. Ergeneman, J. Pokki, F. Ullrich, S. Fusco, J.A. Ortega, K.M. Sivaraman, B.J. Nelson and S. Pané, *Adv. Healthc. Mater.* **4**, 209 (2015).

[3] C. Miao, G. Yang, Z. Bu, X. Lu, L. Zhao, W. Guo and Q. Xue, *Mater. Lett.* **115**, 140 (2014).

[4] J.W. Choi, G.H. Hwang and S.G. Kang, *Met. Mater. Int.* **12**, 81 (2006).

[5] G. Chatzipirpiridis, E. Avilla, O. Ergeneman, B.J. Nelson and S. Pane, *IEEE Trans. Magn.* **50**, 6971759 (2014).

[6] W. Zhang, J. Tian, Y. Wang, X. Fang, Y. Huang, W. Chen, Q. Liu and D. Zhang, *J. Mater. Chem. A* **2**, 4543 (2014).

[7] D. Lelea, S. Nishio and K. Takano, *Int. J. Heat Mass Transfer* **47**, 2817 (2004).

[8] S. Mondal and S. De, *Biomicrofluidics* **7**, 044113 (2013).

[9] K.-J. Lee, D. Tang, K. Park and W.-S. Cho, *Met. Mater. Int.* **16,** 99 (2010).

[10] J. Erlebacher and R. Seshadri, *MRS Bull.* **34,** 561 (2009).

[11] E.S. Toberer, J.P. Löfvander and R. Seshadri *Chem. Mater.* **18,** 1047 (2006).

[12] H. Nakajima and R. Nakamura, *J. Nano Res.* **7**, 1 (2009).

[13] A.J. Smith and D.L. Trimm, *Annu. Rev. Mater. Res.* **35,** 127 (2005).

[14] A.J. Forty, *Nature* **282,** 597 (1979).

[15] S. Rambert and D. Landolt, *Electrochim. Acta* **31,** 1421 (1986).

[16] U.-S. Min and J.C.M. Li, *J. Mater. Res.* **9,** 2878 (1994).

[17] F. Scaglione, E.M. Paschalidou, P. Rizzi, S. Bordiga and L. Battezzati, *Philos. Mag. Lett.* **95,** 474 (2015).

[18] L.D. Gelb, *MRS Bull.* **34,** 592 (2009).

[19] L. Mi, W. Wei, Z. Zheng, Y. Gao, Y. Liu, W. Chen and X. Guan, *Nanoscale* **5**, 6589 (2013).

[20] www.thermocalc.com

[21] http://www.ing.unitn.it/~maud/index.html

[22] Z.-Q. Cao, Y. Niu and F. Gesmundo, *Trans. Nonferrous Met. Soc. China* **11**, 499 (2001).

[23] J.A. Sartell and C.H. Li, *Trans. Am. Soc. Met.* **55**, 158 (1962).

[24] C. Wagner, *J. Electrochem. Soc.* **99**, 369 (1952).

[25] D.P. Whittle and G.C. Wood, *Corros. Sci.* **8**, 295 (1968).

[26] G.W. Castellan and W.J. Moore, *J. Chem. Phys.* **17**, 41 (1949).

[27] A. Atkinson and R.I. Taylor, *Philos. Mag. A* **39**, 581 (1979).

[28] A.D. Smigelskas and E.O. Kirkendall, *Trans. AIME* **171**, 130 (1947).

[29] H. Hokamoto, *Phase diagrams for binary alloys*, ASM International, Metals Park, (2000).

[30] B.D. Cullity, *Elements of X-ray diffraction, 2nd ed.*, Addison Wesley, Reading (1978).

[31] *International Cristallography Diffraction Database (ICDD)*, Reference pattern 01-078-0648.

[32] H. Eric and M. Timucin, *Metall. Trans. B* **10**, 561 (1979).

[33] J.E. Castle and M. Nasserian-Riabi, *Corros. Sci.* **15**, 537 (1975).

[34] R. Souchet, M. Lenglet, P. Miche, S. Weber and S. Scherrer, *Analusis* **21**, 173 (1993).

Figures captions

Figure 1. (a) Optical microscopy images of the cross sections of Cu-44Ni-1Mn (wt.%) wires oxidized at 1173 K in air for different times. (b) Square oxide thickness as a function of the oxidation time for wires oxidized at 1173 K in air. (c) Backscattered electrons SEM image of a cross section of the wire oxidized for 160 minutes at 1173 K in air. (d) EDX elemental map showing the distribution of Cu (red), Ni (green), Mn (blue) corresponding to Fig. 1(c).

Figure 2. (a) XRD patterns (black dots) and Rietveld refinement (red line) of samples after each process step: as received, after oxidation in air at 1173 K for 160 minutes, after etching in HNO_3 and after reduction in H_2 atmosphere (the frequency of the experimental points, black dots, was reduced for graphical reasons). (b) Zoom around the (311) and (222) peaks of the f.c.c. metallic phases related to the wire after reduction in H_2 atmosphere (black dots). Refined patterns are related to f.cc.(1) and f.c.c.(2) phases (green line), eight f.c.c. single phases with different fixed lattice parameters (from blue line to brown line) and the sum of the contributions of the eight f.c.c. phases (red line).

Figure. 3. DSC trace under 10 bar of H_2 atmosphere for a Cu-44Ni-1Mn (wt.%) wire oxidized at 1173 K for 160 minutes and etched in HNO_3.

Figure 4. (a) SEM secondary electrons image of a porous microtube obtained from a Cu-44Ni-1Mn (wt.%) wire oxidized for 160 minutes in air at 1173 K, etched with HNO_3 and reduced under 10 bar of hydrogen. (b) Porous microstructure over the whole width of the tube wall. (c) Porous surface of the inner layer. (d) EDX composition profile of the different elements across the microtube wall.

Fig. 1

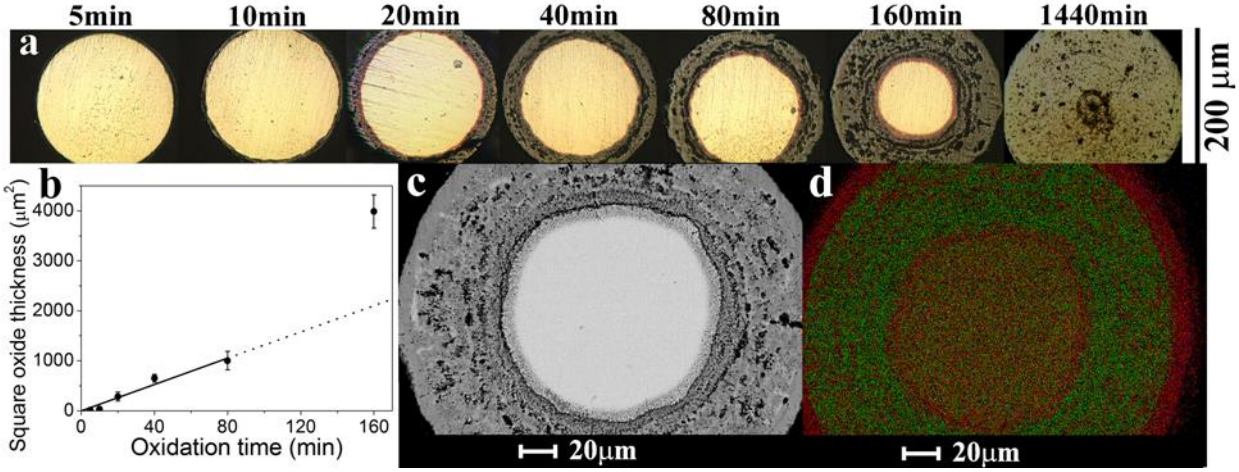
5min
10min
20min
40min
80min
160min
1440min
a
200 μm
b
Square oxide thickness (μm²)
4000
3000
2000
1000
0
0
40
80
120
160
Oxidation time (min)
c
20μm
d
20μm

Fig. 2

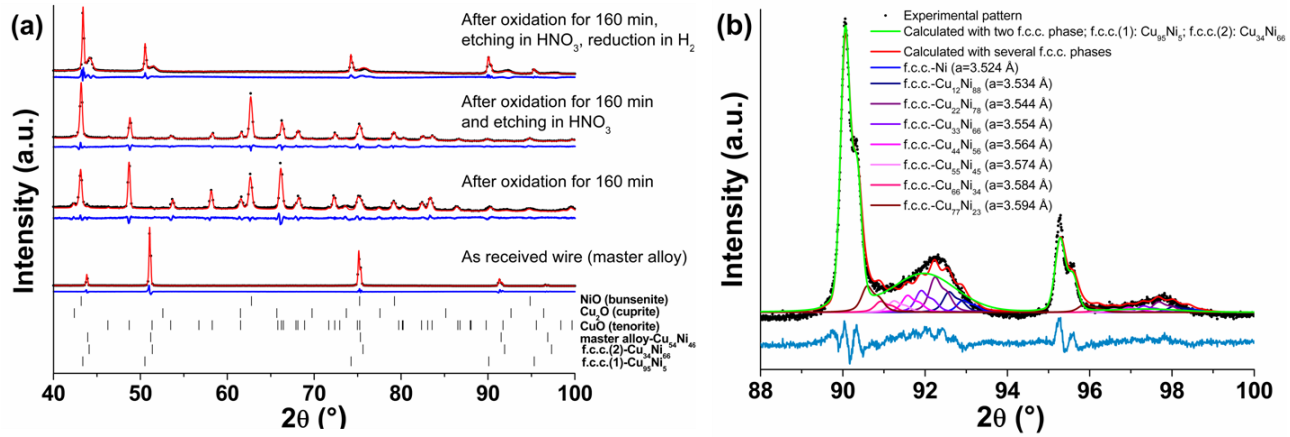
(a)
After oxidation for 160 min, etching in HNO3, reduction in H2
After oxidation for 160 min and etching in HNO3
After oxidation for 160 min
As received wire (master alloy)
NiO (bunsenite)
Cu2O (cuprite)
CuO (tenorite)
master alloy-Cu54Ni46
f.c.c.(2)-Cu34Ni66
f.c.c.(1)-Cu95Ni5
Intensity (a.u.)
2θ (°)
(b)
Experimental pattern
Calculated with two f.c.c. phase; f.c.c.(1): Cu95Ni5; f.c.c.(2): Cu34Ni66
Calculated with several f.c.c. phases
f.c.c.-Ni (a=3.524 Å)
f.c.c.-Cu12Ni88 (a=3.534 Å)
f.c.c.-Cu22Ni78 (a=3.544 Å)
f.c.c.-Cu33Ni66 (a=3.554 Å)
f.c.c.-Cu44Ni56 (a=3.564 Å)
f.c.c.-Cu55Ni45 (a=3.574 Å)
f.c.c.-Cu66Ni34 (a=3.584 Å)
f.c.c.-Cu77Ni23 (a=3.594 Å)
Intensity (a.u.)
2θ (°)

Fig. 3

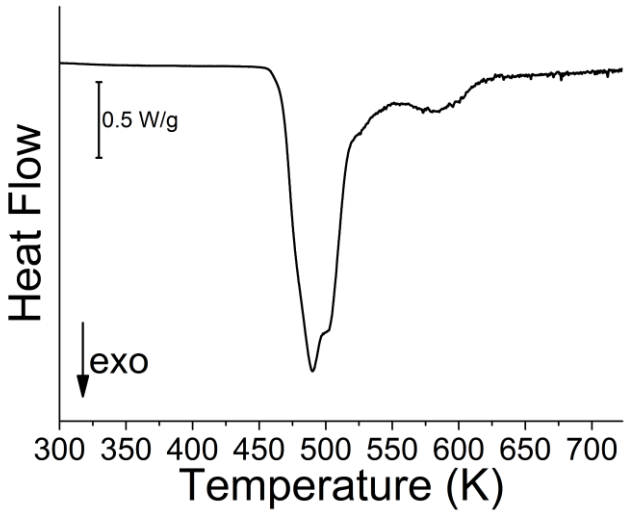
Heat Flow
0.5 W/g
exo
300 350 400 450 500 550 600 650 700
Temperature (K)

Fig. 4

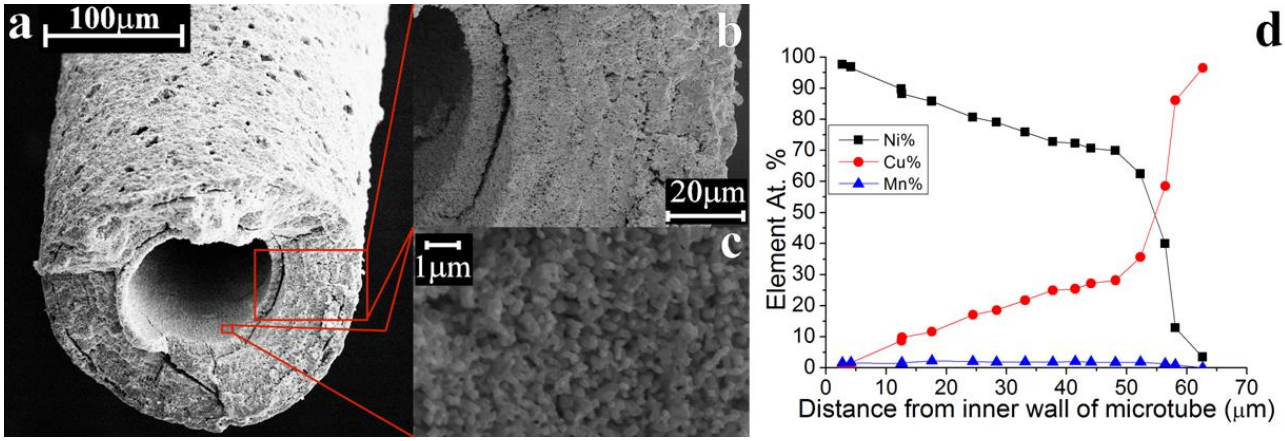
a
100μm
b
20μm
c
1μm
d
Ni%
Cu%
Mn%
Element At. %
Distance from inner wall of microtube (μm)